Research Square

Preprints are preliminary reports that have not undergone peer review.
They should not be considered conclusive, used to inform clinical practice,
or referenced by the media as validated information.

Brain-like adaptive dendritic memristive networks

Gianluca Milano

g.milano@inrim.it

Italian Institute of Metrological Research (INRiM) https://orcid.org/0000-0002-1983-6516

Fabio Michieletti

Politecnico di Torino https://orcid.org/0009-0006-6425-8782

Davide Cipollini

Istituto Nazionale di Ricerca Metrologica (INRiM)

Davide Pilati

Politecnico di Torino

Irdi Murataj

Istituto Nazionale di Ricerca Metrologica (INRiM)

Giuseppe Leonetti

Istituto Nazionale di Ricerca Metrologica https://orcid.org/0000-0002-6281-956X

Gianfranco Durin

Istituto Nazionale di Ricerca Metrologica https://orcid.org/0000-0002-0821-7541

Carlo Ricciardi

Politecnico di Torino https://orcid.org/0000-0002-4703-7949

Ilia Valov

Forschungszentrum Juelich https://orcid.org/0000-0002-0728-7214

Article

Keywords:

Posted Date: September 15th, 2026

DOI: https://doi.org/10.21203/rs.3.rs-10889235/v1

License: This work is licensed under a Creative Commons Attribution 4.0 International License.
Read Full License

Additional Declarations: Yes there is potential Competing Interest. The computing architecture configuration and implementation method are currently under patent filing (Italian priority application number 102026000015787).

Brain-like adaptive dendritic memristive networks

Fabio Michieletti[1,‡], Davide Cipollini[1,‡], Davide Pilati[1,2], Irdi Murataj[1], Giuseppe Leonetti[1], Gianfranco Durin[1], Carlo Ricciardi[2], Ilia Valov[3,4], Gianluca Milano[1*]

[1]*Advanced Materials Metrology and Life Sciences Division, INRiM (Istituto Nazionale di Ricerca Metrologica), Turin, Italy.*

[2]*Department of Applied Science and Technology, Politecnico di Torino, Turin, Italy*

[3]*Forschungszentrum Jülich, Peter Grünberg Institute (PGI-7), Jülich, Germany*

[4]*Institute of Electrochemistry and Energy Systems, Bulgarian Academy of Sciences (BAS), Sofia, Bulgaria*

[‡] *these authors contributed equally to this work*

**e-mail:* g.milano@inrim.it

The remarkable adaptability of biological systems stems from their ability to continuously modify their structural organization in response to experience, making learning an inherently embodied and adaptive process. In contrast, artificial intelligence systems implement learning through the adaptation of connection weights within fixed-topology architectures. This hinders their ability to learn and interact with the environment through adaptive structural reconfiguration. Here we report a brain-like self-organizing hardware architecture that processes information, embeds learning, and stores knowledge directly at the matter level through the co-evolution of structural dynamics and functional connectivity. Leveraging electrochemical mechanisms that emulate synaptic morphogenesis and synaptic plasticity, evolving dendritic structures encode and retrieve spatiotemporal information from the environment as dynamically reconfigurable, engram-like memory traces. This enables the *in-materia* implementation of learning functions directly emerging from material self-organization. Memory-driven adaptation supports associative learning through classical and operant conditioning and solves optimization problems such as path selection for robotic navigation. By bridging information processing, learning, and memory encoding with adaptive materials and physical network dynamics, this work establishes a route toward embodied intelligence at the matter level.

Introduction

The remarkable adaptability of biological intelligence arises from the continual co-evolution of structure and function.[1] Throughout development and learning, biological circuits reorganize their morphology and connectivity through self-organizing processes, allowing information processing, memory, and learning to emerge from the physical dynamics of the network itself.[2,3] In contrast, conventional AI models run on top-down fabricated hardware that acts as a programmable substrate for software-based neural network architectures. The neural network topology is specified at the algorithmic level and mapped onto hardware through software, while learning is implemented through software-based adaptation of connection weights.[4] Although this strategy has enabled remarkable advances in AI, it leaves learning decoupled from the physical evolution of the computing substrate, preventing experience from directly reshaping the computational architecture.

In this context, memristive devices have emerged as promising hardware building blocks because they enable the physical implementation of adaptive synaptic weights through their intrinsic device physics.[5] At the architectural level, top-down fabricated memristive crossbar arrays naturally implement in hardware the weighted bipartite graph connecting adjacent layers in feed-forward artificial neural networks.[6,7] Accordingly, they have been primarily employed as hardware accelerators for deep neural networks by exploiting in-memory matrix–vector multiplication.[6] In these systems, learning is typically implemented through conventional artificial neural network training schemes, relying on error backpropagation and weight-update rules. Training is typically performed *ex situ* and relies on exact or approximate gradient computation together with global error propagation, which is widely considered to conflict with the locality of learning in biological neuronal circuits.[8,9]

From a biologically inspired perspective, memristive architectures based on self-organizing memristive networks have been exploited as adaptive complex systems in which computation emerges from the collective dynamics of many interconnected nano-elements.[10] These systems have been mainly explored within the framework of physical reservoir computing, in which their recurrent and disordered, yet mostly fixed, connectivity provides rich internal dynamics for processing time-dependent input signals, whereas learning occurs outside the physical system through a small set of external readout weights. Consequently, experience is not physically encoded through structural adaptation of the network. To overcome the rigid topologies of conventional hardware, attempts to emulate physical changes in response to input signals have been reported by exploiting electrically induced modification of nanonetworks,[11] electropolymerization-induced dendritic networks of organic electrochemical transistors,[12–15] and guided redox wiring within liquid matrices.[16] However, existing hardware architectures do not physically encode experience through the co-evolution of morphology and functional connectivity within the computing substrate itself.

Here, we report a self-organizing, morphologically adaptive network based on dynamically interacting electrochemical dendrites, in which structural and functional connectivity co-evolve in response to external stimulation. Electrochemical mechanisms that emulate synaptic morphogenesis and synaptic plasticity enable spatiotemporal information to become embedded in the evolving network structure and dynamics as physically instantiated, reconfigurable engram-like memory patterns, supporting both short-term memory dynamics and long-term information storage. We show that these emergent memory states support biological associative learning paradigms - from Pavlovian classical conditioning in dogs to Skinnerian operant conditioning in pigeons and rats - and enable to solve optimization problems such as path selection in a navigation

task. Together, these results demonstrate that material self-organization integrates information processing, memory formation, and adaptive learning within a single physical system, establishing a route toward embodied intelligence at the matter level.

Main

Self-organizing dendrite networks architecture

Neuronal circuits are open systems interacting with the environment that dynamically self-organize, where a global structure emerges from local interactions regulated by mechano-chemical processes and spatial constraints (Figure 1a). The connectivity of these systems relies on the large number of synaptic connections between neurons, which are enabled by their highly branched, tree-like structures that determine their capability to receive and transmit neural signals.[17] The genetic blueprint establishes the foundational topology of these circuits, providing a teleonomic guide, i.e., a mechanism that governs their early structural organization through intrinsic, purpose-oriented developmental forces.[18] Experience then further refines these circuits through activity-dependent structural plasticity that supports learning and memory through modification of the wiring diagram.[9,19–21]

Dendritic arbors and axons are the primary components of neurons, and their morphogenesis determines the wiring diagram of our brain governing fundamental principles of our nervous organization and function. While the morphogenesis of dendritic arbors relies on activity-shaped branching, axon growth is a guided exploration driven by chemical gradients.[22,23] In this view, axonal growth cones navigate chemical potential gradients to connect with dynamically reconfiguring dendritic branches of other neurons. The connection between these components

represents the structural precursor for the formation of synaptic sites, where synapses stabilize and strengthen under correlated (electrical) activity between neurons.

Taking inspiration from the inherent structure-function relation typical of neuronal circuits, we realized an adaptive hardware architecture through electrochemical growth of dendrite networks that self-organize when interacting with the environment (Figure 1b). In these systems, the genetic blueprint typical of biological systems can be mimicked through a programmed blueprint that externally instantiates the pristine morphology of the dendrite network to enhance goal-directed functionalities. The morphogenesis of synaptic connections between neurons, regulated by dendritic arborization and axon growth, was emulated through the dynamic growth of electrochemical dendrites between neuron terminals. Figure 1b schematizes this process in an electrochemical cell composed of Au electrodes taking the role of neurons and a biocompatible $AgNO_3$/dimethyl sulfoxide (DMSO) electrolyte (Methods, Supplementary Section 1). Temporally correlated activity between neuron terminals drives the growth of metallic branches that can structurally connect them to establish electrical junctions (synapses). Indeed, when neuron terminals are stimulated through temporally correlated voltage pulses, described as voltage drops of opposite polarity sequentially applied between them (i.e., a bipolar voltage pulse, Methods), the growth of these dendrites results from the competitive half-cell reactions of the electrochemical cell. The growth process involves the deposition of Ag atoms on the electrode under negative bias (reduction, $Ag^+ + e^- \rightarrow Ag$) and the dissolution of previously formed metallic Ag structures on the electrode under positive bias, releasing Ag^+ ions back to the solution (oxidation, $Ag \rightarrow Ag^+ + e^-$). Under controlled operating conditions, the competition between these two half-cell reactions results in a net growth of dendrites from both terminals due to the asymmetry of growth and dissolution rates involving also the presence of Ag inactive (dead) metal structures, i.e., islands

unconnected from electrodeposited dendrites (Supplementary Section 2). An example of dendritic growth establishing an electrical connection between stimulated neuron terminals is shown in Figure 1c (Supplementary Video 1). The conductance trace, progressively increasing from low- to high-values, correlates with real-time imaging of dendritic evolution characterized by branching, tree-like structures.

This dendritic morphological evolution is explained and modeled through a two-dimensional physics-based stochastic process that integrates the local electric potential at the metal-electrolyte interface and the diffusion transport of ions in the electrolyte. The modeling scheme exploits a separation of time scales. During a single morphological time step, the lattice geometry is held fixed, while the concentration field is allowed to evolve on the faster diffusive time scale. This framework includes capacitive effects arising from the electrical double layer which modifies the local electric potential in the vicinity of the interface between the wetted metal and the electrolyte (Methods, Supplementary Section 3). The model is able to describe both the morphological features of the system and the resulting conductance time trace (Figure 1d, Supplementary Video 2). Experimental and modeling results have confirmed that the growth of dendritic structures relies on the interplay between chemical and electrical driving forces, i.e., diffusion of ions induced by local concentration potential gradients and charge transfer reactions under electric potential guidance. Diffusion-limitations in growth process mirror the approximately isotropic, space-filling branching process underlying dendritic arbor development, in which branches exploratorily extend in multiple directions. The electric potential-limited growth provides directional growth of dendrites towards the counter electrode reflecting the guided, directionally biased exploration characteristic of axon growth. We effectively tune the growth dynamics toward isotropic (dendritic-like) or directional (axon-like) behavior by adjusting stimulation parameters

(Supplementary Section 4). Figure 1e shows that increasing $AgNO_3$ concentration reduces the time required for dendritic connection, also affecting dendrite morphologies (Supplementary Section 5). At fixed concentrations, dendrite growth kinetics can be controlled through pulse amplitude and the interval in between sequential pulses (inter-pulse interval). Experimental and modeled maps of connection time versus pulse amplitude and inter-pulse interval are shown in Figure 1f and g, respectively. Connection time can be reduced *i)* by increasing the stimulation amplitude and/or *ii)* by increasing the temporal correlation in input stimuli (Supplementary Section 6). Connections can be established using pulses from seconds to milliseconds (Supplementary Section 7), with stability exceeding 10^4 s (Supplementary Section 8).

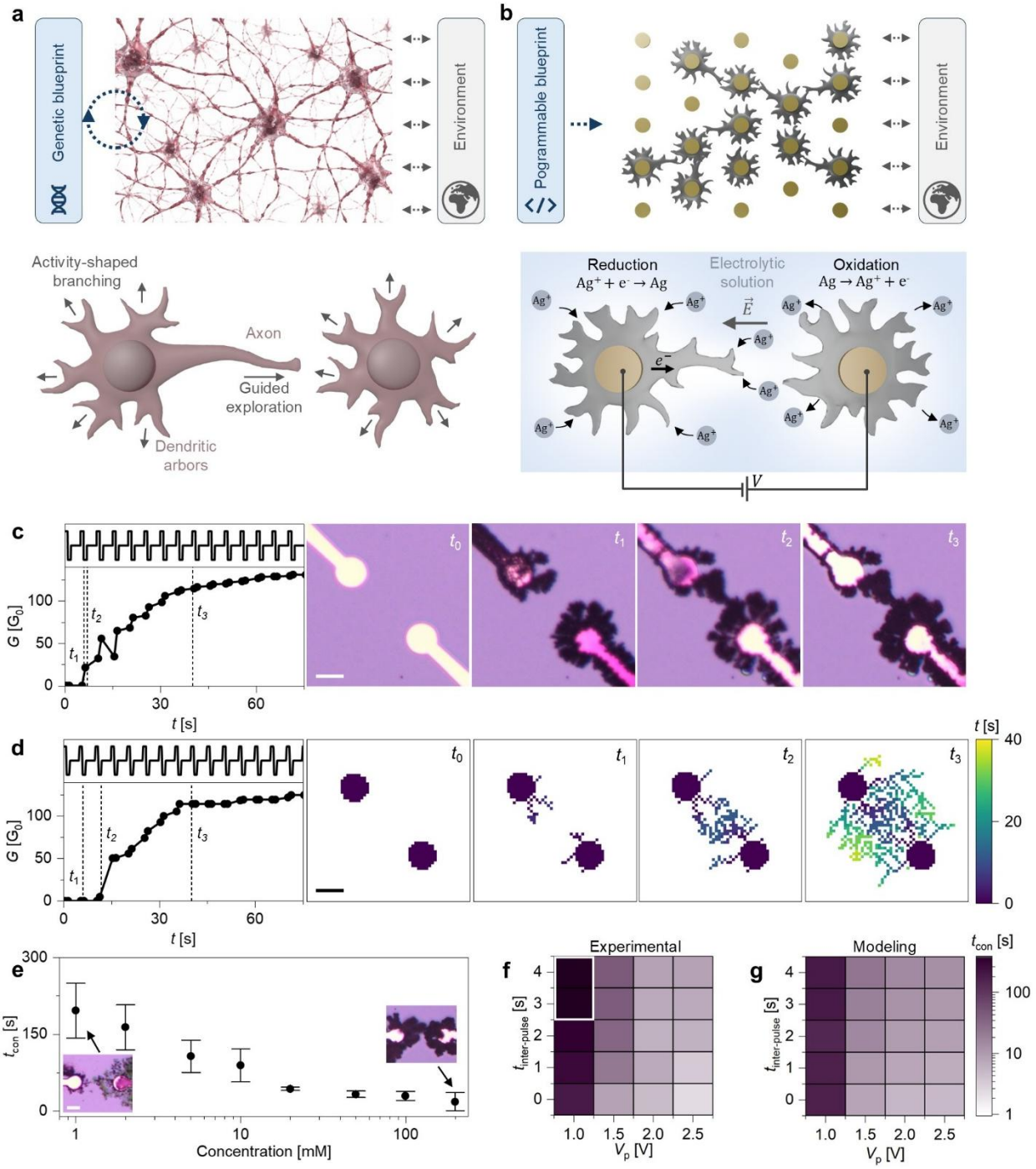


Figure 1 | Morphogenesis of dendrites and synaptic connections. a. Schematic representation of biological neural architectures. The genetic blueprint guides the early structural organization while experience-dependent reorganization refines the neural connectivity. The adaptivity is mediated by phenomena that include dendritic arbors and axon development, characterized by activity-shaped branching and guided exploration, respectively. **b.** Schematic representation of the biologically inspired dendritic architecture. The initial network morphology is defined by an externally programmed blueprint, which establishes a functional backbone for later environment-driven adaptation. The adaptivity is mediated by diffusion-driven (arbor-like) isotropic branching

and potential-driven (axon-like) directional growth governed by concentration and potential gradients. **c.** Experimental and **d.** modeled electrochemical growth of a dendritic connection under bipolar voltage pulse stimulation (2 V, 1 s, time inter pulse of 3 s), characterized by an increase of synaptic conductance over time resulting from the growth of dendrites from neuron terminals, establishment of a synaptic contact and evolution of dendritic morphology over stimulation (scale bar, 10 μm). The enhanced post-connection lateral growth observed in modeling is related to the two-dimensional confinement. **e.** Experimental time required for establishing a connection between dendrites as a function of $AgNO_3$ concentration in the electrolytic solution mean and standard deviation results from the characterization of three different growths for each concentration, performed through stimulation with bipolar voltage pulses (1.5 V, 1 s, time inter pulse of 2 s) (scale bar, 10 μm). **f.** Experimental and **g.** modeled parametric maps reporting the time required for establishing a connection between neuron terminals during bipolar pulse stimulation, as a function of voltage pulse amplitude and temporal correlation in between pulses (inter-pulse time). In panel f, conditions surrounded in white represent situations where the connection was not established after more than 350 s of stimulation time.

Structural plasticity of multiterminal dendrite networks

The stimuli-dependent morphogenesis of dendrites allows the system to embed a spatiotemporal input pattern into a self-organizing network. The possibility of adapting the physical wiring diagram emulates structural plasticity typical of biological systems.[24] Experimental and modeling results for multiterminal network evolution under the stimulation protocol of Figure 2a are shown in Figure 2b and c (Supplementary Video 3), respectively. As can be observed, the network structurally evolves and forms connections between terminals whose activity is spatio-temporally correlated. Co-activated neuron terminals form spatially localized connected components, (e.g., between $t_0 < t < t_1$), and associated neuron terminals progressively diminish their topological distance by reducing their (effective) electrical resistance distance. Depending on the applied potential landscape, multiple dendritic structures can be simultaneously grown in parallel, (e.g., between $t_2 < t < t_3$).

Multiscale network description

The multiterminal system is describable through a multiscale graph-theoretical framework. At a smaller scale representation, each parceled region of the metallic dendrite is treated as a (micrometric) mesoscale node, connected to neighboring regions through edges that encode the local electrical conductance (approach used for modeling, Figure 2c). At this scale, the system is a physical network, whose both nodes and edges are embedded in the physical space.[25] At a larger scale, the evolution of the system's electrical connectivity is represented by a conductance matrix whose elements correspond to the effective conductance between pairs of terminals, measured while all other terminals are left floating (Methods). The terminals thereby define the physically embedded nodes of a graph, while weighted edges are defined by the corresponding effective conductance (experimental and modeling results are shown in Figure 2d and e, respectively, Supplementary Section 9).

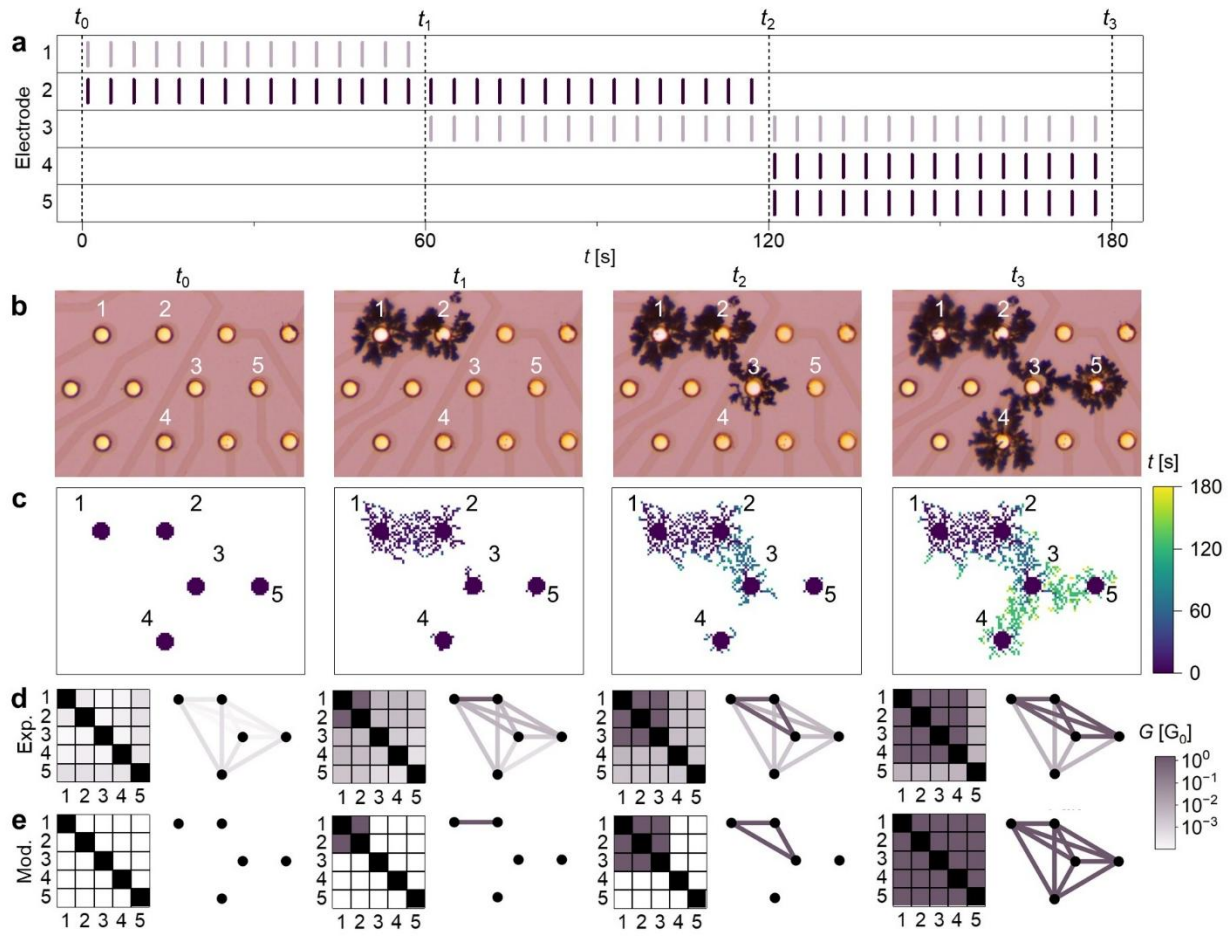


Figure 2 | Structural plasticity and graph-theoretical representation of multiterminal dendrite networks. a. Spatiotemporal input represented as a raster plot. Light purple event markers represent symmetric voltage bipolar pulses where the first is positive (1 V, 1s) and the second negative (-1 V, 1 s), while dark purple event markers represent bipolar pulses with opposite polarity. **b.** Experimental evolution of the structural connectivity of the system, showing the dendritic network morphology at selected timesteps during spatiotemporal stimulation. **c.** Evolution of the structural connectivity of the system obtained through modeling, where the dendrite color reflects the aggregation time of each site. **d.** Experimental and **e.** *in-silico* conductance matrices and corresponding graph representations at selected timesteps. For visualization, experimental conductance values $< 10^{-4}$ G_0 (G_0 is the fundamental quantum of conductance) are mapped to the minimum value of the color scale and displayed using the corresponding minimum colormap. Absence of edges in **e.** reflect no conductance before the establishment of a metallic contact in the model.

Functional plasticity and memristive dynamics

The resulting network forms the structural backbone of a multiterminal memristive system with synaptic connections between dendrites. These synaptic connections are represented by memristive elements where the conductance (synaptic weight) is functionally modified depending on the history of applied stimulation. Indeed, after an initially induced electric breakdown, dendritic connections show bipolar resistive switching behavior typical of memristive devices characterized by the hysteretic loop in the *I-V* plane (Supplementary Section 10). The memristive mechanism shares the same fundamental electrochemical principles underlying resistive switching in electrochemical metallization memory (ECM) cells,[26] characterized by thinning/rupture and formation/strengthening of a conductive filament connecting dendrites depending on the applied voltage (Figure 3a). Unlike conventional (bipolar) ECM cells, both dendrites act as active electrodes, having sufficient number of ions in the electrolyte contributing to channel reinforcement.

Figure 3b shows an example of pulse-controlled memristive switching operations in a dendritic connection. Real-time imaging correlates SET and RESET processes with narrowing and strengthening the connection between the dendrites (Figure 3c, Supplementary Video 4). Besides non-volatile dynamics, dendritic connection can also exhibit volatile behavior, where the functional mode is controlled by the operating conditions (Supplementary Section 11, Supplementary Video 5). Figure 3d provides an example for such short-term memory dynamics. Temporally correlated presynaptic pulses progressively increase the conductance, emulating paired-pulse facilitation (PPF). After the end of stimulation, the connection spontaneously relaxes back to the initial conductance state. This behavior arises from the competition between the electrically driven reinforcement of the connection and its spontaneous dissolution, directed to

minimize the high excess free surface energy.[27] Longer pulse trains convert volatile dynamics into non-volatile long-term memory, where a RESET process is required to return the system back to its initial (low) conductance state (Figure 3e). The dendritic network represents a multiterminal memristive graph[28], whose weighted edges are devised as dynamical variables dependent on the voltage drop across the incident nodes.

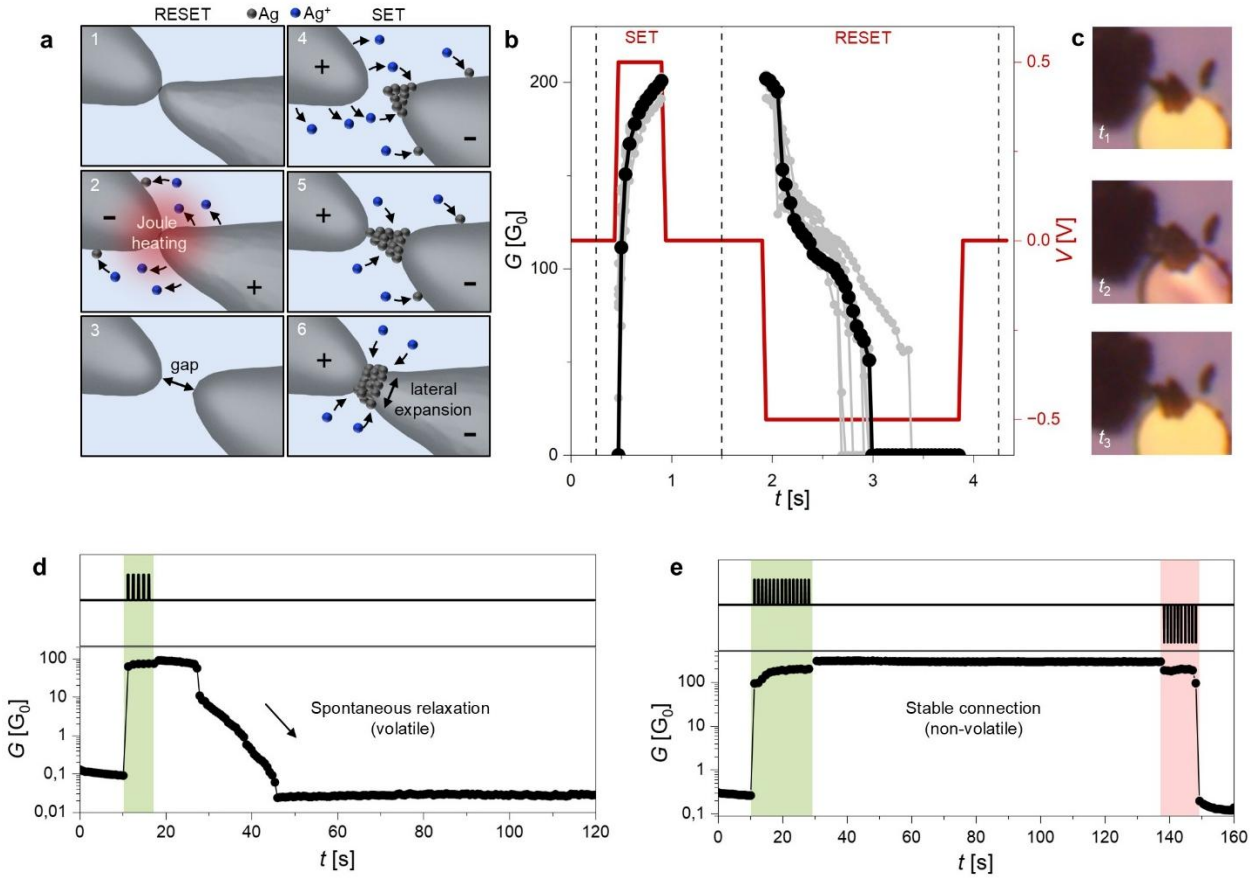


Figure 3 | Functional plasticity and memristive dynamics. a. Schematic representation of bipolar resistive switching mechanism of dendritic connections. The initial dendritic connection (1) is thinned and broken under the application of a voltage through Joule heating and anodic oxidation (2) resulting in the formation of a gap (3) and the transition to the high resistive state. Upon voltage reversal, a filament is formed due to reduction and migration of metallic ions coming from oxidation of the positive potential tip and from the electrolytic solution (4), eventually bridging the gap (5) and setting the system to the low resistive state. The prolonged voltage application successively enlarges the filament, potentiating the electrical connection. **b.** Conductance evolution (greyscale) over 10 cycles under the application of SET and RESET

voltage pulses (red). Dashed lines mark times of interest for the low resistive state and the high resistive state corresponding to optical microscope images of the morphological variation of the thinnest dendritic connection (**c.**). **d.** Conductance time trace (bottom) of the memristive connection in the short-term memory regime. The top panel shows the applied voltage waveform (1 V of pulses magnitude). The green shade marks the set phase. **e.** Conductance time trace (bottom) of the memristive connection in the long-term memory regime. The top panel shows the applied voltage waveform (1 V of positive pulses and -1.5 V of negative ones). Set and reset phases are marked by green and red shades respectively.

Associative learning tasks

The possibility of adapting the structural connectivity of the dendritic network depending on temporal and spatial associations between input signals (structural plasticity) as well as the possibility of changing the weight of the connection between dendrites through memristive dynamics (functional plasticity) enables *in materia* implementation of associative learning principles (Supplementary Section 12). While the structural plasticity enables embedding associations in the network topology, functional plasticity with short-term/long-term synaptic plasticity embeds the finer tuning of the formed association. This makes possible the implementation of both *classical conditioning* based on the association of different stimuli and *operant conditioning* where behavior is associated with consequences through reward/punishing schemes.

Classical conditioning

Classical conditioning is based on the transformation of a neutral stimulus into a conditioned stimulus through repeated temporal synchronization with an unconditioned stimulus.

Pavlov's dog. In Pavlov's dog framework, the dog spontaneously salivates under the sight of food (unconditioned stimulus). On the contrary, bell ringing (neutral stimulus) initially does not elicit salivation. Conditioning is observed when the hearing of the bell and the sight of food repeatedly

occur synchronized. The obtained association between these phenomena turns the bell ringing into a conditioned stimulus, becoming sufficient to trigger salivation alone. The implementation of Pavlov's dog task, where sight of food (F), hearing of the bell (B) and salivation (S) are mapped as stimulation onto distinct terminals, is reported in Figure 4a (Methods, details in Supplementary Section 13). At the pristine state, the F-S association is pre-programmed (programmed blueprint) as a high-conductance dendritic connection encoding the unconditioned response. Then, the task is composed of the following phases (S is set as voltage reference and current output terminal): *i) Before conditioning.* A test phase is exploited for probing S current response under the application of alternated input pulses to F and B terminals. F stimulation causes a significant S response (above the selected 2 μA threshold), confirming unconditioned association between F and S. Conversely, B does not produce significant S output current. *ii) Conditioning.* The process is triggered by the synchronized injection of input pulses to F and B. The resulting dendritic growth topologically bridges these terminals, leading to electrical connections among all the representations. *iii) After conditioning.* A final test phase confirms the association between B and S through the observation of significant output currents under B input pulses. The corresponding evolution of the dendritic network showing the embedding of learned associations is reported in Figure 4b.

Operant conditioning

Operant conditioning is a type of learning based on the reinforcement of a behavior caused by the occurrence of a consequent rewarding stimulus. The seminal research on this field was conducted by B.F. Skinner, who studied this phenomenon by considering the behavior of organisms.[29,30] In the presence of a specific action (e.g., button pressing for rats and pecking of a glowing disk for pigeons), the occurrence of a desirable effect (such as food delivery) causes an increase in the action rate due to the association between these events (*positive conditioning*). In this framework,

the action frequency is modeled as an *operant reserve* (i.e., a reservoir of potential actions) that is expanded by the positive conditioning and is represented by the cumulative sum of action occurrence (Supplementary Section 14). The association can be suppressed owing to two different processes: *i)* the reinforcing stimulus is removed, and the action frequency gradually reduces (*extinction*), *ii)* the reinforcing stimulus is replaced by an undesirable one causing an abrupt frequency reduction (*punishment*). However, the association can be immediately recovered by performing again the original positive conditioning (*periodic reconditioning*). Reassociation occurs faster than initial conditioning and restores, then strengthens, the conditioned action frequency, indicating that extinction and punishment temporarily suppress the behavioral expression of the operant reserve without depleting it. From a neural perspective, part of the information learned is not deleted but silently encoded in brain topology (*savings*).[31] The ability of dendritic systems to reproduce these learning principles is demonstrated by considering Skinner's pigeon pecking[29] and rat punishment tasks[30] (Methods). Here, a reference electrode represents the output behavior, while the other receives from the environment the conditioning signal encoding reward or punishment in a two-terminal configuration.

Pigeon pecking. The setting consists of placing the pigeon in a box with a glowing disk. Each time the disk is pecked, a food ration is released and pecking frequency increases. During extinction (no food supplied), the pigeon gradually stops pecking. When food is supplied again, pecking frequency returns at the original level and is increased, eventually preventing frequency reduction in successive extinctions. Dendritic implementation is shown in Figure 4c and is composed of the following phases: *i) Conditioning.* Rewarding inputs (symmetric voltage pulses) are delivered to the system, causing dendrite growth and bridging of the electrodes. Here, the operant reserve is encoded in the dendrite topology, and the resulting conductance represents the instantaneous

pecking rate. *ii) Extinction.* Rewarding signals are stopped and the system conductance gradually drops to zero. Despite the drop of conductance, dendrite topology is not appreciably varied, indicating a local breaking of dendrites. As a consequence, the stored association is not entirely forgotten and remains structurally embedded (savings). *iii) Reconditioning.* Rewarding pulses are supplied again and the conductance immediately starts increasing to a value higher than the original one. The preformed topology enables to fast recall the original information and to increase the association strength on top of the original one. *iv) Extinction.* As a result, the strongly associated information is not lost during the new extinction phase.

Rat punishment task. The setting consists of placing the rat in a box with a button. As in the previous case, food is delivered each time a button is pressed, until reaching association. For strong conditioning, the button pressing rate is not significantly reduced. In this case, a punishment response (mechanical slap) is delivered after the extinction phase, resulting in an action frequency drop. Even after punishment, the reconditioning is observed to have the same rate of recovery and potentiation effect described for the pigeon task. The task implementation reported in Figure 4d is composed of the following phases: *i) Conditioning.* Rewarding inputs with the same form of the previous task are delivered to the system for a longer period, triggering dendrite bridging. *ii) Extinction.* Removing the rewarding pulses does not cause a significant conductance reduction in time, suggesting a more stable dendritic structure. *iii) Punishment.* Punishment stimuli are delivered to the system in the form of shorter negative pulses and electrical connection is eventually broken (Supplementary Section 15). No significant variations in dendrite topology is observed, maintaining the learned information in the dendritic structure. *iv) Reconditioning.* With a new application of the rewarding pulses, conductance suddenly jumps to values significantly higher than the original one, confirming the recalling of savings and the strengthening effect of

periodic reconditioning. The comparison of results with studies on rat operant conditioning demonstrates that electrochemical dendrites are capable to emulate biological systems responses to operant conditioning (details in Supplementary Section 16).

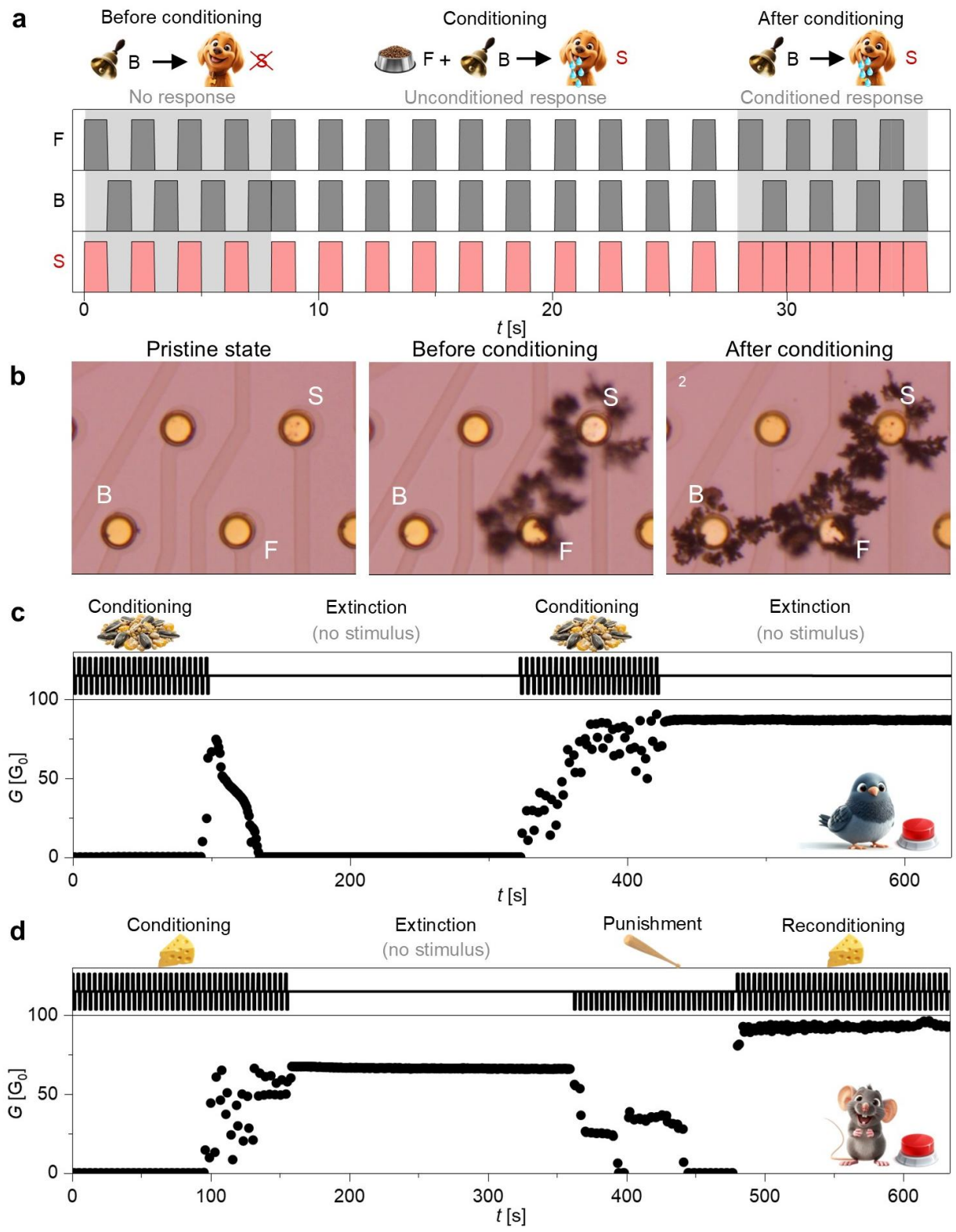


Figure 4 | Associative learning in dendritic networks enabling classical conditioning and operant conditioning tasks. a. Experimental implementation of Pavlov's dog classical

conditioning task in a multiterminal dendritic network. Before conditioning, the food (F) - salivation (S) association is established to represent the unconditioned salivation response to food sight. After this connection is established, salivation is triggered by the food sight but not by the sound of the bell (B) (test phase 1, grey shaded region on the left). Conditioning was performed by associating F and B through synchronous stimulation of corresponding terminals. After conditioning, S is triggered not only by F but also by the B alone (conditioned response) (test phase 2, grey shaded region on the right). F and B stimulation was performed through a square voltage waveform (1 V, 500 ms), while S output was considered to be true in case output current on S terminal overcomes a 2 μA threshold during corresponding F and/or B input. **b.** Corresponding evolution of the dendrite network morphology, including the pristine state, before conditioning, and after conditioning. **c.** Experimental implementation of operant conditioning implementing the Skinner's pigeon pecking task. Conductance time trace (bottom) of the dendritic system under the application of voltage input waveform (top) relative to the conditioning, extinction, and reconditioning phases. **d.** Experimental implementation of operant conditioning implementing Skinner's experiment on the rat punishment task. Conductance time trace (bottom) of the dendritic system under the application of voltage input waveform (top) relative to conditioning, extinction, punishment and reconditioning.

Path selection for robotic navigation

To demonstrate capability of the system to solve optimization problems, we implemented a route-planning task, in which an agent has to identify a route connecting a start location to a target while avoiding regions associated with high traversal costs. This task is relevant, for example, to autonomous robotics, where navigation requires integrating spatial information with local traversal costs. The task has been implemented through modeling, and the setting is reported in Figure 5a, where the presence of sand and rocks on terrain is associated with areas with a higher cost to be traversed by the agent. Solving this task requires the physical system to encode information about the terrain and later retrieve it to guide route selection. To define the ground truth solution, we formulate the route-planning task as a graph-optimization problem, as shown in Figure 5b. The environment is discretized into spatial regions, each assigned a traversal cost based on putative sensor signals that quantifies its local difficulty. Each region corresponds to an electrode in the physical system and to a node in the graph, while graph edges define the allowed transitions between neighboring regions. Candidate routes are therefore paths on the graph, with a cost

functional that combines the total path length with the cumulative cost of traversing regions of different difficulty. The desired solution is the path that minimizes this combined cost, indicated in purple in Figure 5b. This graph formulation is then mapped onto the experimental system by assigning the node costs to the amplitudes of electrical signals represented by node colors in panel b. Such signals are applied at the corresponding electrodes sequentially to encode directional information. In this way, the navigation landscape is converted into a spatiotemporal stimulation protocol shown in Figure 5c that exploits the morphological adaptability of the system (Methods, details in Supplementary Section 17). The corresponding evolution of the dendritic network under spatiotemporal stimulation is reported in Figure 5d (Supplementary Video 6). Under this protocol, the dendritic dynamics transforms the graph constraints into a sparse conductive electrode subnetwork, whose connectivity reflects both the allowed graph topology and the spatial distribution of traversal costs. The growth process therefore acts as a physical sparsifier of the original graph, reinforcing low-cost conductive routes and suppressing high-cost regions. In these terms, dendritic growth embodies and acts as both an analog preprocessing layer and a memory-forming mechanism, generating an ensemble of relevant conductive paths that reduces the effective search space for route extraction.

The final dendrite network encoding the path-finding solution is reported in Figure 5e. Here, the spatiotemporal electrical stimulation protocol enabled storing the information about the terrain as a physical memory in the electrode-to-electrode conductances (Figure 5f). This memory can be retrieved by applying a reading voltage difference between the start and target electrodes. The resulting conductive pathways therefore provide a physical trace of the navigation landscape. This process is reminiscent of engram formation, in which physical changes in neural circuits encode an experience and enable its later recall.[32,33]

In the graph formulation, the ordered sequence of nodes for robot navigation can be retrieved through the conductance matrix of the connected component of the system (Figure 5f) through Dijkstra's algorithm. An average success-weighted overlap of 85% has been measured, where the overlap is defined as the number of edges shared between the extracted path and the ground-truth path normalized by the number of edges of the latter, and further weighted by the fraction of successful conductive connections between the start and target nodes over 25 independent runs (details in Supplementary Section 18). In Figure 5g, the extracted solution paths are overlaid across independent simulations, with edge width proportional to the number of valid simulations in which each edge was included in the extracted path.

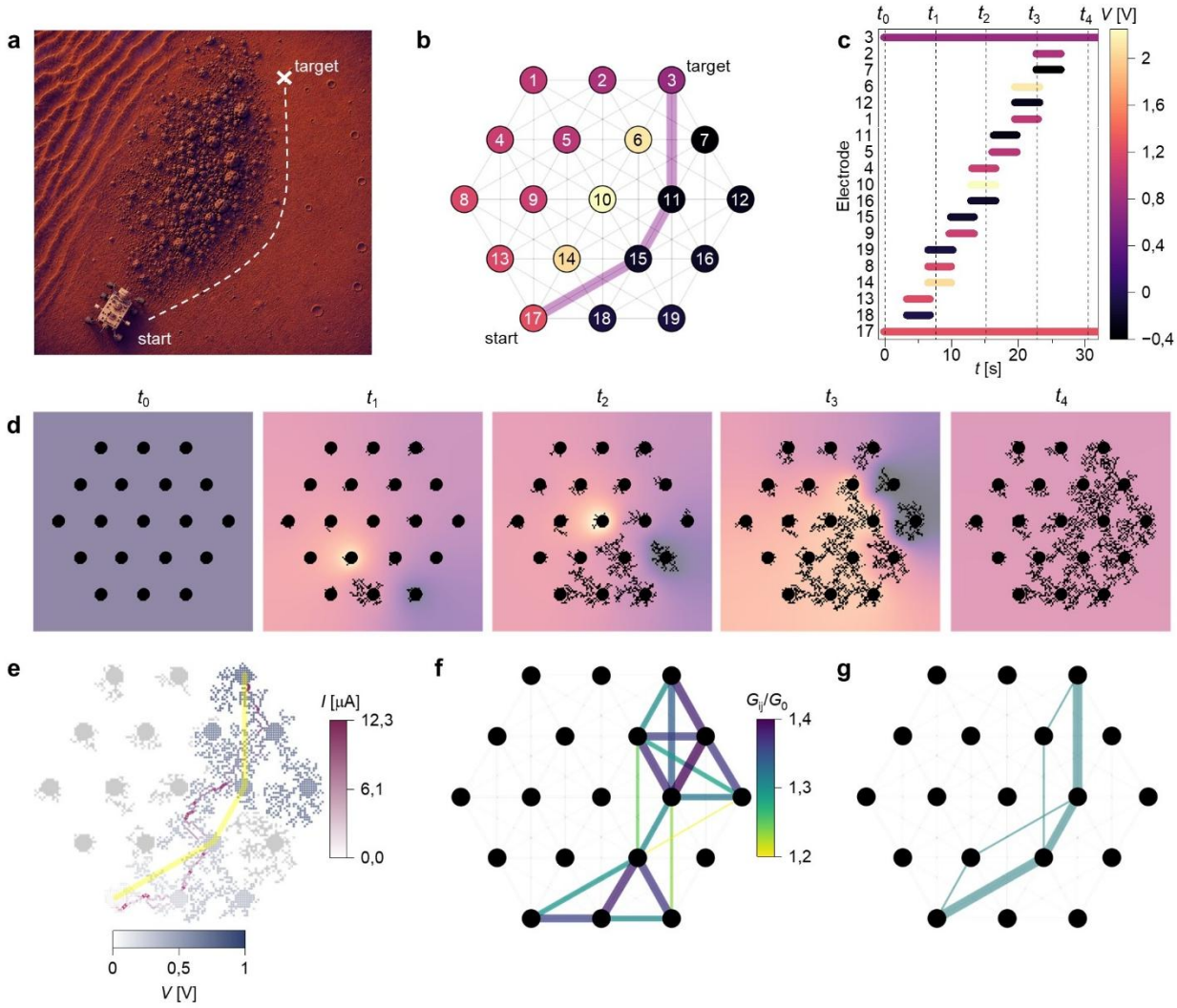


Figure 5 | Path selection for robotic navigation. a. Schematic of the navigation task. A robotic agent has to identify a route connecting a start location to a target while avoiding regions with high traversal difficulty, represented by sand and rocks. **b.** Network representation of the task. Nodes identify discretized regions of the terrain, while edges encode allowed movements between neighboring regions. Node colors indicate the amplitude of the voltage protocol used to encode the local traversal difficulty of the terrain, with the same scale as in panel c. The purple path indicates the ground-truth optimal path. **c.** The terrain-difficulty map is converted into a spatiotemporal stimulation protocol that biases dendritic growth according to the task constraints. **d.** Spatiotemporal evolution of the dendritic network under the protocol shown in panel c obtained through modeling. **e.** Electrical readout of the final dendritic structure. The extracted conductive route is shown by the yellow polyline, indicating the path-finding solution embodied by the grown network. **f.** Reduced electrode graph derived from the electrode-to-electrode conductance matrix of the final dendritic structure. Edge color and width encode the conductance of the filtered graph used to identify the path-finding solution. **g.** Overlay of the extracted conductive paths across 25 independent simulations. Edge width is proportional to the number of valid simulations in which that edge belongs to the extracted solution path.

Discussion

Modern AI systems primarily learn by optimizing connection parameters within pre-engineered, largely fixed architectures, thereby decoupling learning from the physical evolution of the computing substrate. In contrast, we report a physical system in which the computing topology itself adapts during learning. In this system, both functional and structural plasticity coexist within the same physical network, in which the effective computational architecture, connectivity, and transport geometry dynamically reorganize during learning. The activity-dependent growth originates from the structural embodiment of external stimuli through Hebbian learning principles, progressively translating spatiotemporal correlations of input signals into structural connectivity between electrodes. The system embodies the incoming information flow from the environment, and its computational capability emerges intrinsically from material self-organization. Information therefore does not merely propagate through the system but actively shapes and self-organizes the computational structure through which it is processed. Thus, learning can be regarded as the physical embodiment of experience, and computation emerges from the co-evolution of structure and functional connectivity, rather than from parameter optimization alone.

The hierarchical nature of dendritic structures, whose fractal morphology reflects efficient solutions to optimization problems observed across nature at vastly different scales[34], is expected to facilitate a fine balance between segregation and integration of information across the dendritic arbor.[35,36] In electrochemical dendritic networks, stochastic growth promotes exploration, whereas the potential landscape biases growth toward conductive pathways that exploit favorable routes. This interplay mirrors biological networks, which under evolutionary pressure have developed the ability to efficiently distribute resources, maintain robustness against failure, and balance exploration and exploitation during spatial foraging. Such systems have demonstrated remarkable

capabilities in solving combinatorial optimization problems, ranging from maze solving[37] to the emergence of near-optimal transport networks, as exemplified by the Tokyo railway system.[38]

We envision that the associative encoding of spatiotemporally correlated inputs into emergent topological features could enable brain-inspired systems with spatially specialized regions, in which distinct functionalities emerge through experience-dependent structural differentiation. Moreover, this system enables *in materia* exploration of learning principles through the association of memories in the form of partially overlapping distinct dendritic engrams. At the same time, the system may exploit spatial arrangements of learned information to mitigate catastrophic forgetting. Finally, the modeling framework developed here, which captures the underlying physicochemical processes, provides a basis for investigating novel computing paradigms *in silico*, grounded in the thermodynamics of information processing, memory formation, and learning.

Methods

Electrochemical cell and electrolytic solution

The two-terminal electrochemical cells were realised exploiting a standard metal deposition/liftoff process on commercial Si wafer covered by 500 nm thermal silicon oxide (SiMat). Direct laser writing (Heidelberg Laser Writer μPG101) was used to define contacts and electrodes geometries. Before the lithography, substrates were sequentially cleaned in acetone and ethanol for 4 min with the assistance of an ultrasonic bath cleaning system (CEIA CP102) and dried under continuous nitrogen flow. Image reversal AZ5214E photoresist (MicroChemicals GmbH) was spin coated on the substrates and direct laser writing was performed. Samples were developed with AZ 726 MIF (MicroChemicals GmbH) in puddle immersion for 40 s and the development was stopped in bi-distilled water for 30 s. A soft pre-deposition clean was performed in oxygen plasma (Bdiscom PlasmaMatrix) at 40 W and 610-1 mbar for 30 s. Metal deposition was performed in a FC-2000 Temescal FerroTec e-beam evaporator system, 10 nm of Ti and 100 nm Au were sequentially deposited without breaking the vacuum conditions. Standard liftoff process was performed in acetone, with accurate wash in bi-distilled water and dry under continuous nitrogen flow.

Multiterminal electrochemical cells were based on the commercially available microelectrode array chip 60HexaMEA40/10iR-ITO-w/o (Multi Channel Systems MCS GmbH). In this system, ITO contact pads are connected to central TiN electrodes via ITO tracks with resistance of ~ 4.6 kΩ. 200 nm thick Au pins are patterned on top of the TiN electrodes to avoid electrochemical interactions with the electrolytic solutions and maintain comparable growth dynamics to the two-terminal system. Metal deposition and patterning followed the same process described for two-terminal cells.

The electrolytic solutions were prepared by dissolution of $AgNO_3$ in DMSO (≥ 99.9%) for final concentrations of 0.05 M, 0.1 M and 0.2 M (both purchased from Sigma-Aldrich and used without any further purification). The choice of DMSO as solvent enables high solubility of $AgNO_3$ while providing low volatility compared to other commonly employed solvents, low toxicity, and an electrochemical stability window that prevents undesired parasitic reactions that might interfere with Ag redox reactions, as detailed in Supplementary Section 2.

Growth of dendrites

Two-terminal dendrite growth characterization was performed by means of a Keithley 6430 SourceMeter connected to Au pads via micromanipulators. One terminal was used as a reference electrode and set to 0 V, the second one was used to deliver the input voltage signal consisting of bipolar pulses. The applied voltage waveform was formed by repetitions of periods composed of $+V_p$ for 1 s, $-V_p$ for 1s and 10 mV for $t_{inter\text{-}pulse}$. The current was measured with a current range of 1 mA and a current compliance of 1 mA. t_{con} was evaluated as the first instant in which the recorded conductance reaches the threshold value of 1 G_0. Real-time imaging of dendrite growth was carried out through a PS-888L microscope (Seiwa Optical) equipped with an 10X magnifying ocular, a 2X magnifying intermediate lens and an M Plan APO 20X objective lens (Seiwa Optical). Recordings were performed by an AmScope MU500 digital camera.

Multiterminal characterization

Multiterminal measurements were performed using the ArcTWO measurement board, which provides 64 parallel source-measure units (SMU) channels capable of synchronous stimulation and acquisition.[39] The dendritic structures shown in Figure 2 were formed by applying voltage pulse sequences of opposite polarity to selected electrode pairs, generating a sufficient potential drop to activate the underlying redox processes. All other electrodes were kept floating and used as passive voltage probes, following the methodology detailed in ref. [40]. With reference to Figure 2, dendrite growth between electrodes 1 and 2 was initiated by applying the following input voltage signal consisting of bipolar pulses to electrode 1: a +1 V pulse for 1 s, followed by a -1 V pulse for 1 s, and a resting phase at 0 V for 2 s. This cycle was repeated 15 times. Simultaneously, electrode 2 was driven with the same waveform but with inverted polarity. At time $t = t_2$ the same protocol was applied between electrodes 2 (direct polarity) and 3 (inverted polarity), as shown in Figure 2a-b. At $t = t_3$ a branching structure was obtained by applying the protocol to electrode 3 (direct polarity) while simultaneously driving electrodes 4 and 5 with the inverted waveform. During all growth steps, both current and voltage were recorded from the actively driven electrodes, while floating voltage was read from all other electrodes. To track the evolution of the network connectivity, a conductance matrix measurement was performed at $t = t_1$ and prior to each subsequent growth stage ($t = t_2$, $t = t_3$, $t = t_4$; see Figure 2d). The acquisition of the conductance matrix of the multiterminal system exploits the parallel SMU architecture to sequentially address all terminal pairs.[41] For each pair, a low-amplitude read voltage (50 mV) was applied while measuring the resulting current to measure the effective conductance between each pair of terminals. Each 5x5 conductance matrix was acquired in less than 0.2 s using the embedded SMU of the ArcTWO system.

Modeling

The model employed is a discrete two-dimensional representation, where each lattice site exists in either an electrolyte or metallic state. The system is defined on a square lattice with nearest-neighbour and diagonal connections. At every morphological time step, redox events are sampled at the interface between the electrolyte and the metallic clusters. The redox probability depends on the electric potential externally applied on the electrodes and on a dimensionless concentration field. The evolution of the latter is modeled through a reaction-diffusion scheme, taking into account diffusion-limited transport and interfacial ionic mass exchange driven by redox events (see Supplementary Section 3).

The spatial distribution of the electric potential is obtained by solving the discrete Laplace problem using a red-black Gauss-Seidel Successive Over-Relaxation (SOR) method[42] Von Neumann boundary conditions are applied at boundaries of the simulation plate. Dirichlet boundary conditions are imposed on the electrodes and the metallic structure contiguous to them, which evolve over time. Dirichlet conditions are also applied to both dead metals, i.e., metallic islands unconnected from any electrode, and to floating electrodes, fixing their potential to the average potential of the surrounding electrolyte.

The applied potential experienced by the electrolyte is further modulated by the capacitive dynamics of the electrical double layer forming at the interface between the electrolyte and the growing metallic clusters. Consequently, the effective Dirichlet boundary conditions are updated at each time step by solving the corresponding circuit equations with a Backward Euler scheme (details in Supplementary Section 3).

The concentration field introduces diffusion-limited effects through a kinetic limiting factor in the reduction probability. Its evolution is governed by the diffusion equation and solved with a Backward Euler scheme. During reduction events, the concentration update is implemented through a model-specific operator-splitting scheme,[43] in which interfacial consumption and diffusion are treated in separate substeps within a single morphological time step. Newly reduced sites are treated as finite-time interfacial sinks: the local concentration contributes to the reduction event, while the residual demand is supplied by neighbouring electrolyte sites. The lattice geometry is held fixed during this reaction-diffusion subcycling, so that the substeps resolve the competition between interfacial consumption and diffusive replenishment without updating the morphology until the next morphological time step.

The optimization of parameters to determine the dynamics of the two-electrode configuration (see Figure 1) is performed using the standard Differential Evolution algorithm[44] as implemented in Open-Access Python library Scipy.[45] After 10 genetic iterations, model parameters were selected from the saved optimization population using a percentile-based procedure. Individuals with finite objective-function values were ranked by their error, and the best 10% of the population was retained. The final parameter set was obtained by taking the median of each parameter across this selected subset, rather than using the single best individual. The resulting parameter vector was then assigned to the kinetic and electrochemical double-layer model parameters and used in the two-electrode growth simulations. Model parameters exploited in this work are reported in Supplementary Section 19.

Characterization of memristive behavior

Memristive characterization of dendrites was performed with the same setup described for growth characterization. The dendrites were initially grown with bipolar pulses of V_p = 1.5 V and $t_{inter\text{-}pulse}$ = 2 s repeated for 75 periods, with current range and compliance limit set to 1 mA. A first reset process was triggered with a negative voltage ramp with minimum voltage of -2 V, sweep rate of ~90 mV s^{-1}, current range and compliance of 100 mA. For stabilizing the system, 10 IV-sweeps were applied with voltage swinging from - 2 V to 1 V, current range and compliance of 10 mA. Set and reset operations reported in Figure 3b were measured with current range and compliance of 100 mA. The initial reading phase of Figure 3d was obtained by applying a constant 1mV bias with current range and compliance of 10 μA and a sampling interval of 0.6 s for 10 s. Potentiation was obtained with a train of 5 pulses with magnitude of 1 V and 200 ms width separated by 1 s at 1 mV. Current range and compliance were set to 1 mA. The post-pulses reading phase was identical to the pre-pulses one with length of 100 s. Figure 3e characterization was performed starting with a reading phase equal to the previous one. The potentiation phase had the same properties of the Figure 3d one with 10 pulses. Also, the post-pulses reading was identical. The reset pulse train was formed by 10 negative pulses at -1.5 V with a width of 300 ms, inter-pulse periods of 1 s at 1 mV and current range and compliance are set to 100 mA. A final 10 s reading phase identical to previous ones was carried out.

Implementation of associative learning tasks

Pavlov's dog. The task was performed with the same electrical setup described for multiterminal characterization. The F-S association was obtained by applying to the S terminal a +1 V pulse for 0.5 s, followed by a -1 V pulse for 0.5 s, and a resting phase at 0 V for 1 s for 10 periods. The same waveform with inverted polarity was applied to the F terminal, while B terminal was kept floating. After this phase, S terminal was set as a reference electrode (0 V) to read the system output in the

form of current. The output is considered to be true if the output current overcomes the 2 μA threshold during the corresponding input. In the conditioning phase, F terminal received a repetition of its first phase input and B terminal a copy of the first phase S input. Test phases are implemented by applying to the F terminal a -1 V pulse for 0.5 s followed by a +1 V pulse for 0.5 s and a floating phase for 1 s for 4 periods. The B terminal is kept floating when F is stimulated and is stimulated with a+1 V pulse for 0.5 s followed by a -1 V pulse for 0.5 s during the F resting phase. The floating phases prevent each input terminal from influencing the S response under the stimulation of the other one.

Pigeon pecking and rat punishment tasks. The tasks were performed with the two-terminal setup described for dendrite growth characterization. Conditioning was implemented by delivering a growing signal of 1.5 V for 1 s, -1.5 V for 1 s and 10 mV for 2 s repeated 25 times for the pigeon task and 40 times for the rat task. Current range and compliance were set to 1 mA. All the extinction phases were measured with a bias voltage of 1 mV for 200 s at current range and compliance of 10 μA with a sampling time of 0.6 s. The punishment phase was reproduced by applying -1.5 V for 330 ms, 10 mV for 330 ms, -1.5 V for 330 ms and 10 mV for 3 s, repeated for 30 periods (Supplementary Section 15). Current range and compliance were set to 1 mA. Reconditioning was forced by applying the same voltage waveform used for the original conditioning of the relative task.

Implementation of navigation task

The navigation task, implemented through our modeling framework, was encoded on a discrete graph in which each electrode represented a node and neighboring electrodes defined allowed transitions on the physical terrain. The ground-truth path was defined as the minimum-cost path on the baseline graph, with each edge weighted by its unit geometric length plus the mean traversal region-cost relative to the path connecting the two endpoint nodes. The node-cost landscape was then mapped onto the electrochemical stimulation protocol by assigning each electrode an amplitude determined by a contribution from traversal cost of the relative region and an attractive bias toward the target. This voltage landscape was delivered through a plane-wave protocol. Namely, a stimulation front propagated from the start electrode toward the target over 26 s, activating each intermediate electrode with a rectangular voltage pulse of 3.5 s duration. The start and target electrodes were kept active throughout the protocol and up to the end of the simulation window, set here to 45s. The conductance map was then obtained through a virtual electrical readout of the frozen morphology at the selected time point. Specifically, a 1 V potential difference was imposed between the start and target electrodes only as a boundary condition to solve the electrical problem and compute the electrode-to-electrode conductance. In the simulations, this readout step does not update the lattice, concentration field, or dendritic morphology; it therefore probes an instantaneous property of the system state. The use of a 1 V readout is also consistent with the experimental results in Figure 2, where this voltage amplitude does not induce appreciable morphological changes over the relevant timescale.
The readout was performed 4s after the first appearance of a conductive connection between the start and target electrodes, allowing the newly formed conductive pathway to further consolidate before evaluation. The electrode-to-electrode conductance matrix was converted into a reduced conductance graph by retaining only the links of the baseline graph whose corresponding conductance was non-zero in the simulated readout matrix. Each retained edge was assigned a readout cost inversely proportional to its conductance. In an experimental implementation, where residual leakage currents and instrumental noise can lead to finite background conductance values,

the same criterion should be replaced by a conductance threshold, retaining only edges with conductance above the noise floor. The final path was extracted from this active physical sub-network using Dijkstra's shortest-path algorithm and compared with the ground-truth solution using an edge-overlap metric. A detailed description of task implementation is provided in Supplementary Section 17.

Author contributions

F.M., D.C., and G.M. generated the idea and designed the experiments. F.M. performed experimental activities, D.C. performed modeling activities. D.P. and I.M. supported experimental activities, G.L. supported device fabrication, G.D. supported simulation activities. F.M., D.C., and G.M. performed data analysis. I.V. supported interpretation of results. F.M., D.C., and G.M. wrote the manuscript. G.M. supervised the research. All authors participated in the discussion of results and revision of the manuscript.

Competing interests

The computing architecture configuration and implementation method are currently under patent filing (Italian priority application number 102026000015787).

Acknowledgements

This project has received funding from the European Research Council (ERC) under the European Union's Horizon Europe research and innovation programme (ERC Starting Grant "MEMBRAIN", Grant Agreement No. 101160604). Views and opinions expressed are however those of the authors only and do not necessarily reflect those of the European Union or the European Research Council. Neither the European Union nor the granting authority can be held responsible for them.

References

1. Fotiadis, P. *et al.* Structure–function coupling in macroscale human brain networks. *Nat. Rev. Neurosci.* **25**, 688–704 (2024).
2. Suárez, L. E., Richards, B. A., Lajoie, G. & Misic, B. Learning function from structure in neuromorphic networks. *Nat. Mach. Intell.* **3**, 771–786 (2021).
3. Hedrick, N. G. *et al.* Learning binds new inputs into functional synaptic clusters via spinogenesis. *Nat. Neurosci.* **25**, 726–737 (2022).
4. LeCun, Y., Bengio, Y. & Hinton, G. Deep learning. *Nature* **521**, 436–444 (2015).
5. Tang, J. *et al.* Bridging Biological and Artificial Neural Networks with Emerging Neuromorphic Devices: Fundamentals, Progress, and Challenges. *Advanced Materials* **31**, (2019).
6. Xia, Q. & Yang, J. J. Memristive crossbar arrays for brain-inspired computing. *Nat. Mater.* **18**, 309–323 (2019).
7. Huang, Y. *et al.* Memristor-based hardware accelerators for artificial intelligence. *Nature Reviews Electrical Engineering* **1**, 286–299 (2024).
8. Crick, F. The recent excitement about neural networks. *Nature* **337**, 129–132 (1989).
9. Lillicrap, T. P., Santoro, A., Marris, L., Akerman, C. J. & Hinton, G. Backpropagation and the brain. *Nat. Rev. Neurosci.* **21**, 335–346 (2020).
10. Caravelli, F. *et al.* Self-organising memristive networks as physical learning systems. *Nature Review Physics, Accepted Manuscript* (2026).
11. Milano, G. *et al.* Brain-Inspired Structural Plasticity through Reweighting and Rewiring in Multi-Terminal Self-Organizing Memristive Nanowire Networks. *Advanced Intelligent Systems* **2**, (2020).
12. Janzakova, K. *et al.* Structural plasticity for neuromorphic networks with electropolymerized dendritic PEDOT connections. *Nat. Commun.* **14**, (2023).
13. Janzakova, K. *et al.* Analog programing of conducting-polymer dendritic interconnections and control of their morphology. *Nat. Commun.* **12**, 6898 (2021).
14. Scholaert, C., Coffinier, Y., Pecqueur, S. & Alibart, F. Brain-Inspired Polymer Dendrite Networks for Morphology-Dependent Computing Hardware. *Advanced Science* **12**, (2025).
15. Cucchi, M. *et al.* Reservoir computing with biocompatible organic electrochemical networks for brain-inspired biosignal classification. *Sci. Adv.* **7**, eabh0693 (2021).
16. Terasa, M.-I. *et al.* Pathways towards truly brain-like computing primitives. *Materials Today* **69**, 41–53 (2023).
17. Sehgal, M. *et al.* Compartmentalized dendritic plasticity in the mouse retrosplenial cortex links contextual memories formed close in time. *Nat. Neurosci.* **28**, 602–615 (2025).
18. Monod, J. *Chance and Necessity: Essay on the Natural Philosophy of Modern Biology*. (1971).
19. Holtmaat, A. & Svoboda, K. Experience-dependent structural synaptic plasticity in the mammalian brain. *Nat. Rev. Neurosci.* **10**, 647–658 (2009).

20. Lamprecht, R. & LeDoux, J. Structural plasticity and memory. *Nat. Rev. Neurosci.* **5**, 45–54 (2004).
21. Tronel, S. *et al.* Spatial learning sculpts the dendritic arbor of adult-born hippocampal neurons. *Proceedings of the National Academy of Sciences* **107**, 7963–7968 (2010).
22. Rosoff, W. J. *et al.* A new chemotaxis assay shows the extreme sensitivity of axons to molecular gradients. *Nat. Neurosci.* **7**, 678–682 (2004).
23. Vitriol, E. A. & Zheng, J. Q. Growth Cone Travel in Space and Time: the Cellular Ensemble of Cytoskeleton, Adhesion, and Membrane. *Neuron* **73**, 1068–1081 (2012).
24. Caroni, P., Donato, F. & Muller, D. Structural plasticity upon learning: regulation and functions. *Nat. Rev. Neurosci.* **13**, 478–490 (2012).
25. Pósfai, M. *et al.* Impact of physicality on network structure. *Nat. Phys.* **20**, 142–149 (2024).
26. Valov, I., Waser, R., Jameson, J. R. & Kozicki, M. N. Electrochemical metallization memories—fundamentals, applications, prospects. *Nanotechnology* **22**, 289502 (2011).
27. Valov, I. *et al.* Nanobatteries in redox-based resistive switches require extension of memristor theory. *Nat. Commun.* **4**, 1771 (2013).
28. Milano, G. *et al.* Memristance and transmemristance in multiterminal memristive systems. *Sci. Rep.* **16**, 5271 (2026).
29. Ferster, C. B. & Skinner, B. F. *Schedules of Reinforcement*. (Appleton-Century-Crofts, East Norwalk, 1957).
30. Skinner, B. F. *The Behavior of Organisms:An Experimental Analysis*. vols ix, 457 p. ill. (New York, London, D. Appleton-Century company, incorporated, 1938).
31. Ryan, T. J., Roy, D. S., Pignatelli, M., Arons, A. & Tonegawa, S. Engram cells retain memory under retrograde amnesia. *Science (1979).* **348**, 1007–1013 (2015).
32. Frankland, P. W., Josselyn, S. A. & Köhler, S. Engrams. *Current Biology* **34**, R559–R561 (2024).
33. Milano, G., Cultrera, A., Boarino, L., Callegaro, L. & Ricciardi, C. Tomography of memory engrams in self-organizing nanowire connectomes. *Nat. Commun.* **14**, 5723 (2023).
34. Ball, P. *Nature's Patterns : A Tapestry in Three Parts. Branches*. (Oxford ; New York : Oxford University Press, 2009).
35. Cipollini, D. & Schomaker, L. Tree networks of real-world data: Analysis of efficiency and spatiotemporal scales. *Phys. Rev. Res.* **7**, 033009 (2025).
36. Makarov, R., Pagkalos, M. & Poirazi, P. Dendrites and efficiency: Optimizing performance and resource utilization. *Curr. Opin. Neurobiol.* **83**, 102812 (2023).
37. Nakagaki, T., Yamada, H. & Tóth, Á. Maze-solving by an amoeboid organism. *Nature* **407**, 470–470 (2000).
38. Tero, A. *et al.* Rules for Biologically Inspired Adaptive Network Design. *Science (1979).* **327**, 439–442 (2010).
39. Foster, P. *et al.* An FPGA-based system for generalised electron devices testing. *Sci. Rep.* **12**, 13912 (2022).

40. Pilati, D., Michieletti, F., Cultrera, A., Ricciardi, C. & Milano, G. A Multiterminal Setup for Complex Dynamics Characterization and Unconventional Computing in Self-Organizing Memristive Networks. in *2025 IEEE International Conference on Metrology for eXtended Reality, Artificial Intelligence and Neural Engineering (MetroXRAINE)* 1236–1241 (IEEE, 2025). doi:10.1109/MetroXRAINE66377.2025.11340466.
41. Pilati, D., Michieletti, F., Cultrera, A., Ricciardi, C. & Milano, G. Emerging Spatiotemporal Dynamics in Multiterminal Neuromorphic Nanowire Networks Through Conductance Matrices and Voltage Maps. *Adv. Electron. Mater.* **10**, (2024).
42. Young, D. M. *Iterative Solution of Large Linear Systems*. (Elsevier, 2014).
43. MacNamara, S. & Strang, G. Operator Splitting. in *Splitting Methods in Communication, Imaging, Science, and Engineering* 95–114 (Springer, Cham., 2016). doi:10.1007/978-3-319-41589-5_3.
44. Storn, R. & Price, K. Differential Evolution – A Simple and Efficient Heuristic for global Optimization over Continuous Spaces. *Journal of Global Optimization* **11**, 341–359 (1997).
45. Virtanen, P. *et al.* SciPy 1.0: fundamental algorithms for scientific computing in Python. *Nat. Methods* **17**, 261–272 (2020).

Supplementary Files

This is a list of supplementary files associated with this preprint. Click to download.

- DescriptionofSupplementaryVideos.docx
- SupplementaryVideo1.mp4
- SupplementaryVideo4.mp4
- SupplementaryVideo2.mp4
- SupplementaryVideo6.mp4
- SupplementaryVideo3.mp4
- SupplementaryMaterial.docx
- SupplementaryVideo5.mp4